




# The impact of different surfactants on the structure, surface area, and electrochemical properties of hydrothermally synthesized spinel NiCo<sub>2</sub>O<sub>4</sub> nanoparticles

A. Abu El-Fadl<sup>1,2,\*</sup> , Mohaned M. M. Mohammed<sup>1,2</sup>, Heba R. Mansour<sup>1,2</sup>, A. M. Nashaat<sup>1,2</sup>, and Gh. Abbady<sup>2</sup>

<sup>1</sup> Smart Materials for Energy Future Research Laboratory, Department of Physics, Faculty of Science, Assiut University, Assiut 71516, Egypt

<sup>2</sup> Physics Department, Faculty of Science, Assiut University, Assiut 71516, Egypt

Received: 16 April 2022

Accepted: 13 January 2023

Published online:

21 February 2023

© The Author(s) 2023

## ABSTRACT

NiCo<sub>2</sub>O<sub>4</sub> Nanoparticles have been synthesized by a facile hydrothermal method followed by annealing at a temperature decided based on differential thermal (DTA). Different additives and surfactants were used in preparation under the same synthesis conditions and their effects on the physical properties of spinel nickel cobaltite nanoparticles have been investigated in a fair comparison study. The synthesis products have been characterized by using DTA and TGA measurements, X-ray diffraction, scanning electron microscopy, transmission electron microscopy, and Fourier transform infrared spectroscopy. Modification on the synthesis of the spinel nanoparticles provided high specific capacitance of 2253 F g<sup>-1</sup> at 1 A g<sup>-1</sup> and long-term cyclic stability for 10,000 cycles with 90% capacitance retention.

## 1 Introduction

Spinel nickel cobaltite, NiCo<sub>2</sub>O<sub>4</sub>, has been extensively studied in nanostructured form over the last three decades due to its enhanced electronic conductivity and much high electrochemical activity compared to those of nickel and cobalt oxides that extended its usage in supercapacitor applications [1]. A lot of research has been devoted to the synthesis of nickel cobaltite in different forms and the development of

their properties to match such applications in asymmetric supercapacitors [2, 3], flexible fiber hybrid supercapacitors [4], electrochemical glucose sensor [5], and as a bifunctional electrocatalyst for water-splitting and oxygen reduction [6, 7]. NiCo<sub>2</sub>O<sub>4</sub> belongs to the spinel structured compounds with the general formula AB<sub>2</sub>O<sub>4</sub>, with A being a divalent transition metal ion while B is a trivalent transition metal such as Al<sup>3+</sup>, Fe<sup>3+</sup>, Cr<sup>3+</sup>, or Co<sup>3+</sup> [8]. Among these spinel ferrites, nickel cobaltite exhibits an

Address correspondence to E-mail: abulfadla@aun.edu.eg; abulfadla@yahoo.com

inverse spinel structure, due to the large stabilization energy with Ni in the B site, and shows a ferrimagnetic transition well above room temperature [9]. The cation redistribution and coexistence of di- and trivalent Ni and Co in the magnetic p-type  $\text{NiCo}_2\text{O}_4$  with tunable electrical, optical, and magnetic properties, make it a versatile candidate for spintronics and energy storage applications.

In recent years, the demand for energy storage devices with low cost, eco-friendly, stable, and long life has grown in the industry and academic fields. The supercapacitor has a wide scope in different fields like transportation, wearable devices, electronics, and other fields for energy storage due to its exclusive electrochemical features like fast charge-discharge activity, high specific power, and long cyclic stability [10, 11]. The supercapacitor stores energy in various ways according to the storage mechanism. The two types of supercapacitors are electric double-layer capacitors (EDLC) and pseudocapacitors (PCs) [11]. Energy stored in EDLC is based on charge separation at the interface between the electrode and the electrolyte. Carbon materials like graphene, graphene oxide, carbon nanotubes, and multiwall carbon tubes show EDLC storage mechanisms. In pseudocapacitors, the energy is stored according to the redox process in most metal oxides, metal chalcogenide, and conducting polymers, which shows the PCs' mechanism to store energy [12, 13].

$\text{NiCo}_2\text{O}_4$  exhibits promising pseudocapacitance behavior due to the low resistance exhibited by  $\text{NiCo}_2\text{O}_4$  than those of NiO and  $\text{Co}_3\text{O}_4$  separately and richer sites contribution from both cobaltite and nickel oxides to high capacitance [14]. The redox reaction in  $\text{NiCo}_2\text{O}_4$  is enhanced by multiple oxidation states of nickel cobaltite thus storing more charges. These outstanding characteristics disclose the improvement of  $\text{NiCo}_2\text{O}_4$  as a promising electrode material for supercapacitors. The microstructure of the electrode material is strongly affecting the electrochemical performance, which includes the porosity and specific surface area [15, 16].

$\text{NiCo}_2\text{O}_4$  has been synthesized with various structures, such as porous nanowires, mesoporous nanosheets, hierarchical hollow nanocubes, hierarchical tetragonal microtubes, hollow spheres, and

urchin-like microspheres, and they exhibit a distinct difference in their electrochemical performance [8]. Therefore, changing the synthesis method has a major effect on the final materials, and it is extremely important to choose an appropriate synthesis route to control the characteristics developed for different applications. A lot of methods have been used to synthesize nickel cobaltite nanoparticles with desirable features for the facile process commonly including microwave [17], hydroxide decomposition [18], sol-gel [19], electro-deposition [20], co-precipitation [21], and combustion method [22]. Most of these synthesis routes have control on some effects in the resultant samples, like faces or surface area, size of pores, crystallinity, structure, etc. [6]. One of the methods that are proven with good merits and are largely used is the hydrothermal method [23–25].

In this study, the hydrothermal method was used to prepare spinel  $\text{NiCo}_2\text{O}_4$  nanoparticles and the effect of adding different surfactants on the structure and physical properties of nickel cobaltite was studied by several techniques. Three-electrode cell system was used to investigate the electrochemical performances of the synthesized electrodes.  $\text{NiCo}_2\text{O}_4$  nanoparticles prepared by adding surfactants/additives demonstrate high electrochemical performance for usage as a supercapacitor electrode material.

## 2 Experimental techniques

### 2.1 Synthesis

In a typical synthesis of  $\text{NiCo}_2\text{O}_4$  nanoparticles, 2.6 mmol of  $\text{NiCl}_2 \cdot 6\text{H}_2\text{O}$  and 5.2 mmol of  $\text{CoCl}_2 \cdot 6\text{H}_2\text{O}$  were mixed with 41.6 mmol of urea and dissolved in 35 ml distilled water to obtain a homogenous solution using a magnetic stirrer. The solution was then transferred to a 50-ml Teflon-lined stainless-steel autoclave. The hydrothermal reaction took place at a fixed temperature of 120 °C for 6.5 h, and then, the sample was air-cooled down to room temperature. The resultant precipitate was filtered out and washed several times, first with distilled water and acetone to obtain a controlled precursor. The filtered precursor was then dried at ambient temperature.

The same steps were followed with one selected additive from ammonium fluoride (AF),

cetyltrimethylammonium bromide (CTAB), polyvinyl alcohol (PVA), polyvinyl pyrrolidone (PVP), polyethylene glycol (PEG-4000), or triethanolamine (TEA), added as a surfactant/additive to the fixed atomic ratio of 1:2:12 for Ni/Co/Urea to form the mixture solution. The surfactant ratios were estimated based on the molecular weight as detailed in the supplementary material. The synthesized precursor samples are labeled in Table 1. Precise weights and details of the synthesis are described in section S1 of the supplementary file.

The hydrothermal reaction does not directly give the spinel oxide phase in one step and the precursors are almost hydroxide-based phases. The thermal analysis was performed on the control precursor sample after drying at ambient temperature to investigate the optimum annealing temperature for the formation of the NiCo<sub>2</sub>O<sub>4</sub> phase. Based on the thermal analysis described below, all precursors have been annealed at 350 °C for 5 h to provide a thermally stable NiCo<sub>2</sub>O<sub>4</sub> spinel nanoparticles.

## 2.2 Characterization methods

To investigate the decomposition processes of the prepared precursors, differential thermal analysis (DTA) and thermogravimetric analysis (TGA) were carried out using SHIMADZU simultaneous DTA-TG apparatus with DTG-60H detector with standard error  $\pm 1^\circ$ ; the powder samples were placed in an aluminum cell under nitrogen followed by heating at a rate of 10°/min.

X-ray powder diffraction has been collected using Philips X-ray diffractometer model PW 1710 with CuK<sub>α</sub> radiation ( $\lambda = 1.5405 \text{ \AA}$ ) with an operating applied voltage of 40 kV and current of 30 mA. The scanning rate was maintained at 0.06° per minute, in the 2θ range of (4°–80°). FTIR spectroscopy has been performed on the samples using NICOLET FTIR 6700 spectrometer by employing the KBr pellet method, in the wavenumber range 400–4000 cm<sup>-1</sup>. Scanning electron microscopy (SEM) apparatus, (JSM)-T200 Jeol-Japan, was used to investigate the surface

morphology of the powder samples. Elemental analysis was determined using ESEM FEI QUANTA 250FEG (FEI, Hillsboro, OR, USA) with an Oxford EDX (energy dispersive X-ray spectrometer) instrument (Oxford Instruments, Tubney Woods, UK). For further investigation, transmission electron microscope (TEM) images are observed by JEOL (JEM-2100 Electron Microscope, USA).

The Brunauer–Emmett–Teller (BET) method was used to determine the specific surface area. Prior to the measurement, the sample was degassed at 250 °C for 2 h under vacuum. Then, the adsorption–desorption isotherms of the samples were measured using N<sub>2</sub> at –196 °C with a Quantachrome surface area/pore size analyzer NOVA 3200e.

Electrochemical testing was measured by a CHI 760E potentiostat in a 6.0 M KOH electrolyte using a three-electrode system. The working electrodes were prepared by dissolving the NiCo<sub>2</sub>O<sub>4</sub> nanoparticles, carbon black, and polyvinylidene fluoride (PVDF) binder (ratio 80:10:10) in *N*-Methyl-2-pyrrolidone (NMP) to form a paste. Then, the paste was pressed into an NF current collector and dried at 120 °C overnight. Pt plate of 1 × 1 cm<sup>2</sup> was used as a counter electrode, and Ag/AgCl electrode was employed as a reference electrode. Cyclic voltammetry (CV) was performed between 0 and 0.6 V at scan rates of 2, 5, 10, 20, 50, and 100 mV s<sup>-1</sup>. Galvanostatic charging/discharging (GCD) was measured between 0 and 0.4 V at current densities of 1, 2, 5, 10, 15, 20 A g<sup>-1</sup>. The specific capacitance was estimated from the CV curves as follows [26]:

$$C_m = \frac{\int IdV}{sm\Delta V} \quad (1)$$

where  $I$  represents the current,  $s$  denotes the scan rate,  $\Delta V$  expresses the potential window, and  $m$  is the active material mass.

The specific capacitance was estimated from the GCD curves as follows [11, 13]:

$$C_m = \frac{i\Delta t}{\Delta Vm} \quad (2)$$

**Table 1** Summary of the sample's codes throughout the manuscript

Additive/surfactant	None	PVA	PVP	AF	CTAB	TEA	PEG-4000
Label	NC-Control	NC-PVA	NC-PVP	NC-AF	NC-CTAB	NC-TEA	NC-PEG

where  $i$  denotes the discharging current,  $\Delta t$  represents the discharging time,  $\Delta V$  expresses the potential range, and  $m$  represents the loading mass of the active material on NF.

The electrochemical impedance spectroscopy (EIS) was measured in the frequency range from 10 mHz to 100 kHz at open circuit potential with an amplitude of 10 mV.

### 3 Results and discussion

#### 3.1 Thermal analysis

DTA and TGA curves of the control  $\text{NiCo}_2\text{O}_4$  sample precursor are presented in Fig. 1. The TGA curve shows a slightly steep weight loss corresponding to the lattice water removal within the temperature range (60 °C–280 °C). A drop around 280 °C is observed with weight loss that starts to fade around 318 °C. This drastic weight loss is attributed to the decomposition of the binary hydroxide. The corresponding DTA curve shows two thermal reactions: one exothermic peak centered at 234 °C and an endothermic peak centered at 304 °C. The DTA curve describes the thermal treatment of the sample and makes initiative information on the start temperature of decomposition. Similar results are reported by Yang et al. [27]. The control sample prepared under these conditions is not thermally stable below 320 °C and it does not show any thermal activity at and above 350 °C as depicted from the DTA curve. Hence,

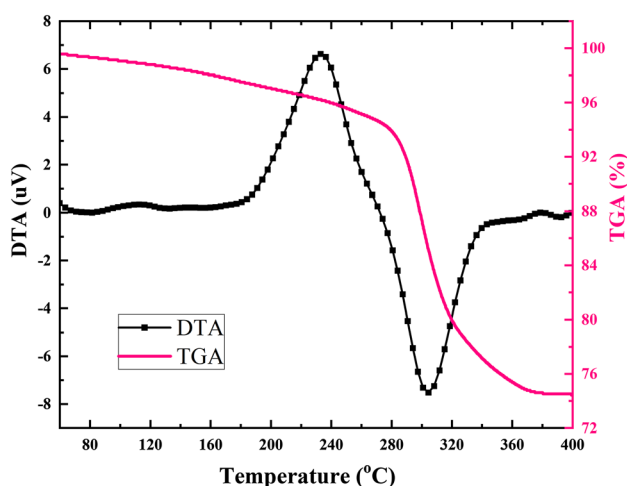


**Fig. 1** DTA/TGA curves of the  $\text{NiCo}_2\text{O}_4$  (control) precursor sample

the data suggest an appropriate annealing temperature for the control precursor samples at 350 °C to provide a thermally stable  $\text{NiCo}_2\text{O}_4$  spinel based on the thermal analysis report.

The TGA curves for precursor samples prepared with different surfactants are displayed in Fig. 2i and ii. The figures show a slight shift with using different surfactants, the common weight loss corresponding the decomposition occur at a temperature range between 280 and 320 °C. The as-prepared samples with NC-PVA, NC-PVP, and NC-AF surfactants show weight loss characteristics like the control precursor sample with sharp decomposition loss starts at about 280 °C, with slight shift to higher temperature. Precursors with other surfactants show the main weight loss as shown in Fig. 2ii, with a steep over

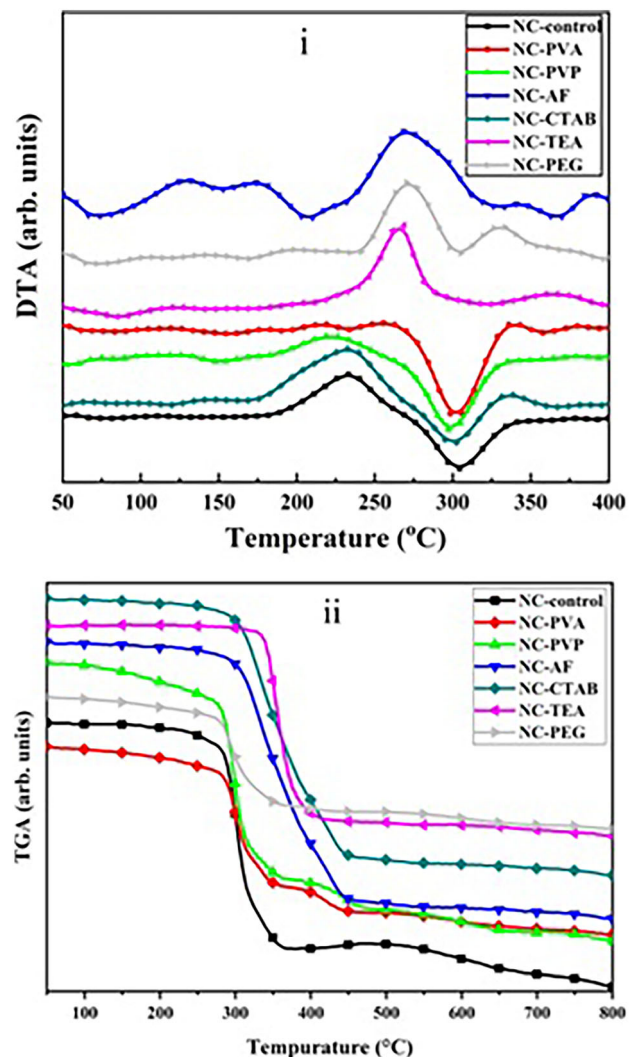


**Fig. 2** Thermal analysis curves of the prepared  $\text{NiCo}_2\text{O}_4$  With samples i—DTA, ii—TGA



wider range of temperature. For example, the NC-AF precursor sample shows TGA curve with almost no weight loss up to  $\sim 300$  °C followed by a decomposition loss occurring at higher temperature.

The DTA curves of the precursor samples prepared with a surfactant are depicted in Fig. 2i. Thermal behavior different from that of the controlled precursor is observed with some different characteristics among samples prepared with different surfactants/additives. These changes in thermal behavior may be due to the complexes formed during the hydrothermal reaction with organic ligands attached to the structure. To establish a fair comparison, the thermal results are shown separately in two graphs. Figure 2 shows that both NC-PVP and NC-CTAB develop the same endo- and exothermic peaks observed in the control precursor and almost at the same positions which means that the surfactants PVP and CTAB do not develop new organic ligands that affects the thermal stability of the resultant powder. The NC-PVA sample does not show a diminished exothermic peak instead of the pronounced peak for the control sample. However, it shows the endothermic peak around 318 °C. The other precursor samples prepared with surfactant exhibit distinct DTA curves. From a glance to Fig. 2, it appears that the surfactants/additives used in these samples develop additional organic ligands or different complexes during the hydrothermal reaction. The DTA curve of the NC-AF precursor shows different thermal events in the temperature range 50–250 °C which can be attributed to a relaxation of the fluoride–hydroxide complex. The big exothermic peak shown around 270 °C can be attributed to the decomposition and formation of the oxide phase. Zhan et al. [28] described similar effects of ammonium fluoride in the synthesis of NiO nanoparticles. NC-TEA precursor sample shows one sharp exothermic peak around 270 °C. The sharp exothermic peak and the good thermal stability observed in TGA curve of NC-TEA sample indicate the formation of weaker organic ligands around the binary hydroxide which required small energy to decompose [27]. The NC-PEG sample is developed by using polyethylene glycol PEG-4000. This sample exhibits two exothermic peaks. The variations in the DTA and TGA curves of NC-PEG may be related to the molecular weight of PEG and the chain length [29].

Based on the results of thermal analysis, the prepared precursor samples contain different ligand

complexes after the hydrothermal reaction without and with different surfactant. An appropriate annealing temperature at 350 °C can be selected to decompose the precursor into stable oxide spinel phase. Although the extended TGA analysis up to 800 °C (Fig. 2ii) showed that all samples do not exhibit major weight loss after 450 °C, yet most of the samples are stable below this temperature. The suggested annealing temperature is nominated as the lowest possible temperature to produce stable nanoparticles for all the samples with minimum particle size and thermal stability, as the suggested temperature exceeds the onset of the major weight loss for all samples.

### 3.2 Structural analysis

Powder x-ray diffraction (PXRD) was employed to identify the phases developed in the annealed  $\text{NiCo}_2\text{O}_4$  samples. As deduced from the thermal analysis, the spinel  $\text{NiCo}_2\text{O}_4$  oxide phase can be obtained after thermal treatment of the powder above 300 °C. The annealing duration was fixed at 5 hours to provide sufficient degree of crystallization and ensure the elimination of any residuals that may result from the different additives/surfactants used in the synthesis process as explained in the thermal analysis section. The PXRD spectra were analyzed and refined to determine the effect of additives/surfactants on the structural and microstructural parameters.

The Rietveld refinement of the PXRD pattern has been performed using FULLPROF software [30]. The refinement of the control  $\text{NiCo}_2\text{O}_4$  nanoparticles is presented in Fig. 3. The structure is refined to the cubic spinel  $Fd\bar{3}m$  structure with structural details reference from the ICDD PDF file 04-021-8094. The refinement confirmed the formation of spinel cubic structure of  $\text{NiCo}_2\text{O}_4$  in good agreement with references [31–34]. No other additional peaks of diffraction or other phases are observed, indicating that high purity  $\text{NiCo}_2\text{O}_4$  nanoparticles are obtained after a simple annealing process.

As presented in Fig. 3, the calculated pattern matches well the observed powder diffraction pattern. The refined lattice constant and the related PXRD parameters are tabulated in Table 2. The unit cell parameters calculated from the diffraction pattern is visualized using VESTA software [35] and presented in the inset of Fig. 3. The calculated value of the

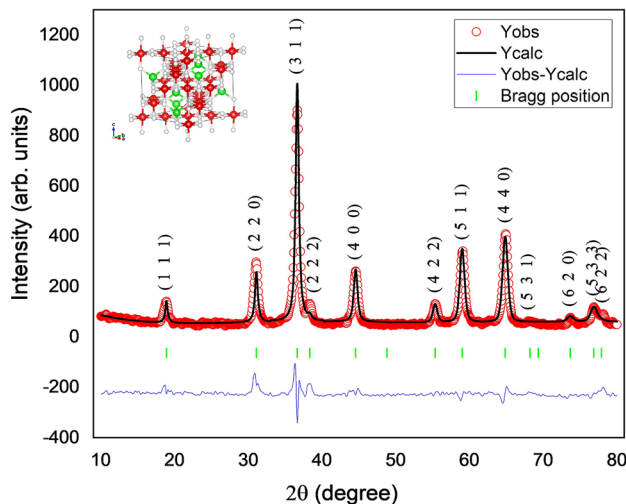


**Fig. 3** Rietveld refinement of the XRD pattern of  $\text{NiCo}_2\text{O}_4$  nanoparticles (control sample) annealed at  $350\text{ }^\circ\text{C}$ . The refined unit cell deduced from powder diffraction pattern is presented (red: Co, green: Ni, gray: oxygen)

lattice constant,  $8.131\text{ \AA}$ , is slightly lower than the reported values in the PDF card, while the occupancy of the atoms is altered with respect to minimum thermal parameters in the unit cell.

The annealed samples from precursors with surfactant (hereafter, denoted as modified samples) were thermally treated and measured under identical conditions as those for the control sample. The PXRD pattern of the whole system is presented in Fig. 4. From the first glimpse, the samples appear to develop a well-defined peaks of spinel cubic phase and show the same crystallographic reflections. Figure 4 infers that the modification by a surfactant or an additive does not affect the cubic spinel structure after the same thermal treatment. The PXRD patterns of the control and modified samples show small differences in intensity and some apparent shift in the peak

**Table 2** Structure parameters obtained by Rietveld refinement of the PXRD patterns for the  $\text{NiCo}_2\text{O}_4$  spinel nanoparticles

Sample	$a$ ( $\text{\AA}$ )	Volume ( $\text{\AA}^3$ )	$D$ (nm)	$\varepsilon \times 10^{-5}$
NC-Control	8.1311	537.563	11.983	- 11.17
NC-PVA	8.1031	532.048	13.739	2.461
NC-PVP	8.1279	536.960	13.254	16.86
NC-AF	8.1174	534.868	14.116	7.613
NC-CTAB	8.0936	530.179	16.520	15.96
NC-TEA	8.0950	530.454	15.609	16.77
NC-PEG	8.1202	535.418	14.546	1.701

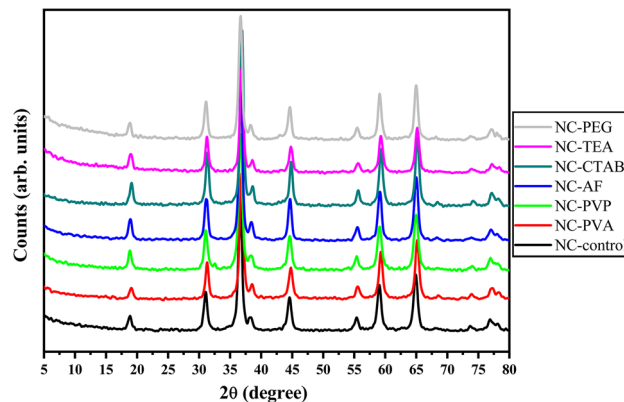


**Fig. 4** XRD spectra of the annealed  $\text{NiCo}_2\text{O}_4$  nanoparticles treated with different additives/surfactants

positions which can be attributed to a slight change in the unit cell volume and development of different lattice strain. The small variations in the peaks' width, shape, and shift were predicted from the thermal analysis and after applying unified thermal treatment overall the samples despite their different thermal behavior. But the thermal annealing duration was proved to be sufficient for the development of the spinel nanoparticles at this temperature without any noticeable traces or residuals recorded in the PXRD patterns.

The calculated values of the lattice constant based on PXRD data analysis are tabulated in Table 2. The NC-control sample exhibits the largest unit cell volume when compared with the other samples. NC-CTAB and NC-TEA show the minimum value of the unit cell volume.

The microstructure of the PXRD is analyzed using Williamson–Hall (W–H) model to calculate the average particle size and the unit cell strain from the broadening of the PXRD peaks [36]. The broadening of the PXRD peaks of the different samples consists of the instrumental broadening and the particle size broadening, that can be described by the equation:

$$\beta_{\text{size}}^2 + \beta_{\text{instrumental}}^2 = \beta_{\text{measured}}^2 \quad (3)$$

where  $\beta$  is the FWHM of the PXRD peaks. To use the W–H model, the instrumental broadening must be excluded from the measured broadening. The average instrumental broadening was estimated from the standard Si diffraction pattern measured using the same setting and apparatus.

The average crystallite size  $D$  and lattice strain  $\varepsilon$  are estimated using the W–H model according to the equation:

$$\beta_{hkl}\cos\theta = \frac{K\lambda}{D} + 4\epsilon\sin\theta \quad (4)$$

where  $K$  is constant set to 0.9 and  $\lambda$  is the wavelength of the X-ray used (0.15406 nm, Cu target).  $D$  and  $\epsilon$  are obtained by linear fitting of a plot between  $\beta\cos\theta$  versus  $\sin\theta$  for all reflections as detailed in the supplementary material. The calculated values of the particle size and lattice strain are presented in Table 2.

The average crystallite size varies between 12 and 16 nm for the prepared samples with the minimum value for NC-control. The smallest value of the crystallite size for the NC-control sample corresponds the maximum unit cell volume. The lattice strain in nanoparticles resembles the contraction or expansion of the unit cell due to the size confinement. The estimated negative value of lattice strain in this sample may be ascribed to an anisotropy component of the strain which affects the overall strain of the unit cell. Another explanation may be due to the chemical pressure in unit cell which may arise from cations redistribution between the tetrahedral and octahedral sites [37].

Another typical behavior is observed for the NC-CTAB and NC-TEA samples which have the maximum particle size and minimum unit cell volume. Among the prepared samples, NC-PVA, NC-AF, and NC-PEG exhibit low values of lattice strain, such values are independent on their particle size and unit cell volume values. The lattice strain values can be related to the measure of the defects, as size confinement produces defects in the unit cell and in turns that produces a strain.

### 3.3 FTIR spectroscopy

The FTIR spectra for NiCo<sub>2</sub>O<sub>4</sub> nanoparticles are recorded in the wavenumber range 4000–400 cm<sup>-1</sup>. Normally, the characteristic vibrational bands of the spinel oxides develop at the lower values of wavenumber. Figure 5 shows the FTIR spectra with the characteristic vibration bands in the range between 800 and 500 cm<sup>-1</sup>. The first indication from the spectra is the confirmation of the spinel structure for the prepared samples.

The relative positions of the observed vibrational bands for the prepared samples are presented in Table 3. The two characteristic bands are assigned to the stretching vibration  $\nu_2$  of B–O bond mainly

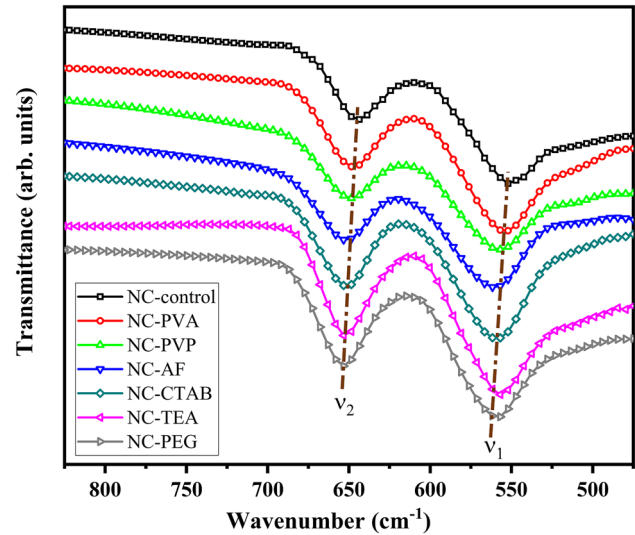


Fig. 5 FTIR spectra for the synthesized NiCo<sub>2</sub>O<sub>4</sub> nanoparticles

located at the octahedral sites and the stretching vibration  $\nu_1$  of A–O bond at the tetrahedral sites. The positions of the vibrational bands for the prepared samples are approximate to the positions observed for spinel cobalt chromites [38] and cobalt oxide Co<sub>3</sub>O<sub>4</sub> [39]. While the bands for the NC-Control, NC-PVP, and NC-AF samples seem to be broadened than the rest of the samples. All the samples with surfactant demonstrate a slight shift in position. These variations in the FTIR curves can be attributed to the surface defects resulted from using different surfactants/additives.

The force constant of the cations in the tetrahedral and octahedral sites  $K_T$  and  $K_O$ , respectively, can be calculated from the following relation [40]:

$$K_{T/O} = 4\pi^4 C^2 v^2 \mu \quad (5)$$

where  $C$  is the speed of light in cm s<sup>-1</sup>,  $\mu$  is the reduced mass of Co<sup>+3</sup> and O<sup>-2</sup> ( $\sim 2.09 \times 10^{-23}$  g), and  $v$  is the vibrational frequency. The calculated force constants are listed in Table 3. The estimated force constant from FTIR spectra varies by the sites of (Co<sup>+3</sup>–O<sup>-2</sup>) ions due to the different ionic radii of Co–O distances on octahedral and tetrahedral sites. As the force constant is proportional to the square of vibration frequency. It is clearly observed that the force constant values in tetrahedral sites are less than those at octahedral sites. Both values are slightly higher in samples with surfactant with slightly diminished lattice volume.

**Table 3** FTIR parameters for the prepared NiCo<sub>2</sub>O<sub>4</sub> nanoparticles

Sample	$\nu_1$ (cm <sup>-1</sup> )	$\nu_2$ (cm <sup>-1</sup> )	$K_T \times 10^5$ (dyne cm <sup>-1</sup> )	$K_O \times 10^5$ (dyne cm <sup>-1</sup> )
NC-Control	550	644	2.2463	3.0798
NC-PVA	553	647	2.2709	3.1085
NC-PVP	558	648	2.3122	3.1182
NC-AF	560	652	2.3288	3.1568
NC-CTAB	559	651	2.3204	3.1471
NC-TEA	557	652	2.3039	3.1568
NC-PEG	559	653	2.3204	3.1665

### 3.4 Morphology and microstructure

The morphology of the prepared samples was investigated by the electron scanning microscope (SEM) and the micrographs for the prepared samples are presented in Fig. 6. The micrographs report the direct effect of different surfactants/additives on the surface morphology of the particles. All the micrographs for different samples are presented at the same magnification ratio for the sake of fair comparison (Fig. 6). Different magnifications which demonstrate an overall view of the samples are illustrated in Fig. S2.

The main observation from the micrographs is that the particles form to some extent uniform shaped particles aggregate. Typically, the control sample shows what we may call semi-sphere morphology which consists of round edges and porous structure. Similar morphology is noticed for NC-PVA and NC-CTAB samples with variations in the radial size and uniformity. The NC-PVP sample develops well-defined microspheres with porous surface. NC-PEG sample shows traces of microsphere but with more agglomeration, nanoparticles which are shown clearly in the micrograph forming a wide porous background.

The samples with unique morphologies are NC-AF and NC-TEA. The sample NC-AF showed an agglomeration of nanoneedles with random orientations and different diameters, but they are clearly defined in the micrograph. NC-TEA sample showed an interesting morphology as the particles appear to be a continuous surface with small porosity when compared to the rest of the samples. For larger magnification of the sample (Fig. S2), the particles form well-defined geometrical shapes with sharp edges like cubes or in general regular polyhedron. The presented micrographs highlight the effect of different surfactants/additives as the resulted morphologies depend on the type of the additive and the concentrations. As the study conducted a comparison

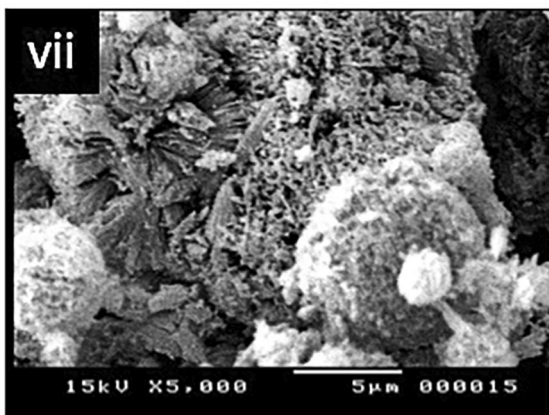
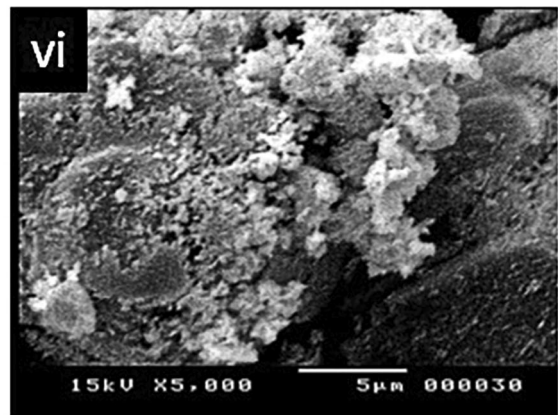
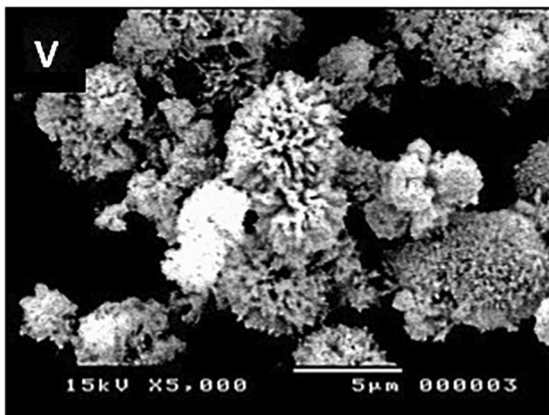
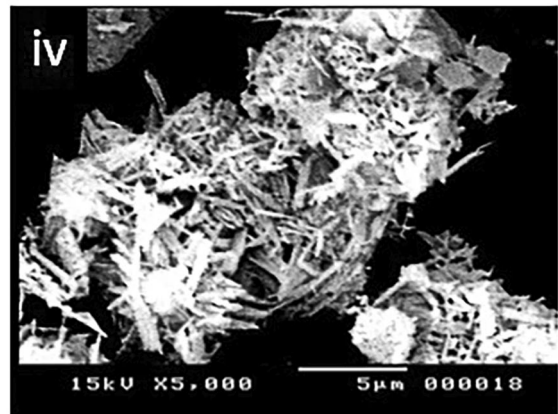
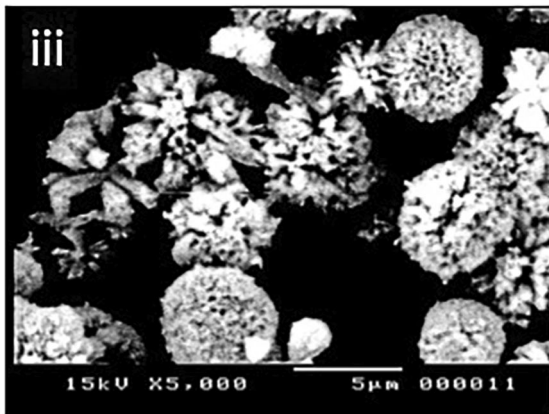
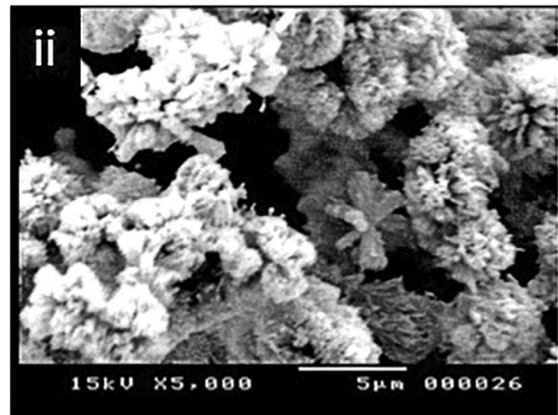
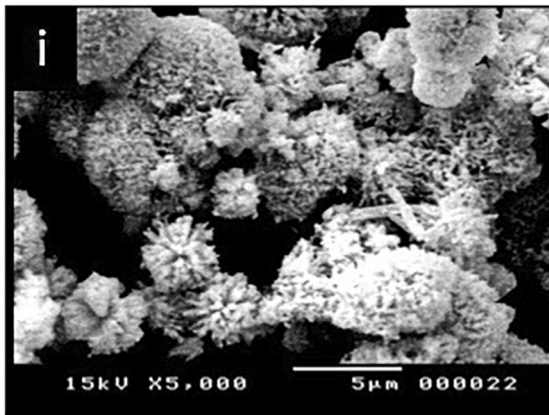
between different types of additives with low concentrations, the effect can be purely justified by the composition of the additive itself. Thus, the apparent variations between the samples could be due to the variety of the additives employed in the study, except for PVP and PVA which converge to similar but not identical morphology.

### 3.5 Elemental and microstructure analysis

The particle size distribution of the NC-control and NC-PVP samples was investigated using HR-TEM, and the micrographs are presented in Fig. 7. The images presented at the same magnification ratio to provide a fair argument on the effect of PVP on the nanoparticle size. The histogram of the control sample presented in Fig. 7i shows that the average particle size of the control sample is around 16 nm corresponding to the center of the normalized curve. In addition, the particles show low tendency for stacking, but the particles are well defined but with soft edges. NC-PVP sample gives bigger average particle size  $\sim$  21 nm as extracted from the histogram shown in Fig. 7ii. The PVP addition increased the average particle size, and the normalization curve peak is shifted toward higher average particle size. The crystallinity on the other hand is improved and agglomeration of particles are frequent and indicated as dense areas with geometrical sharp edges. The TEM micrographs of NC-control and NC-PVP samples suggest that at the same preparation conditions, the addition of PVP to the reaction precursor enhanced the growth rate of NiCo<sub>2</sub>O<sub>4</sub> nanoparticles and affected the geometrical shape of these particles.

The surface mapping of the NC-control and NC-PVP samples is presented in Fig. 8. The mapping of elements over different areas of the sample can give qualitative results on the concentration of each element but upon a certain depth depending on the apparatus and the accelerating voltage and other





◀ **Fig. 6** SEM micrographs for the prepared samples at analogous magnification. i—Represents the magnification over the control sample, from ii- to vii- for NC-PVA, NC-PVP, NC-AF, NC-CTAB, NC-TEA, and NC-PEG, respectively

parameters concerning the sample preparation. Yet it can provide important information on the elemental concentration and their distribution over the sample surface. Figure 8i shows the mapping of Ni, Co, and O over a large portion of the control sample. The mapping micrographs show a homogenous distribution of the elements with higher concentration for Co and O when compared with Ni which consents with the chemical formula of  $\text{NiCo}_2\text{O}_4$ , there are no noticeable area where atoms can be seen exclusively.

Same observation is found for the NC-PVP sample in shown Fig. 8ii. The EDX spectra are presented in Fig. 8. The EDX spectra presented in Fig. 8 are indexed to the corresponding energy for the main elements under consideration (Co, Ni, and O) for different excitation levels K and L, while the additional peaks in the spectra can be attributed to the sample holder material, adhesives used to stick the powder on the holder and carbon traces from the coating of the sample. The calculated elemental concentrations are tabulated in Table 4. The results do not represent the actual concentrations of elements overall the samples but at the surface of the samples, which is the interest for electrochemical application. The main observation from the mapping analysis is that the PVP sample demonstrates an increase in the

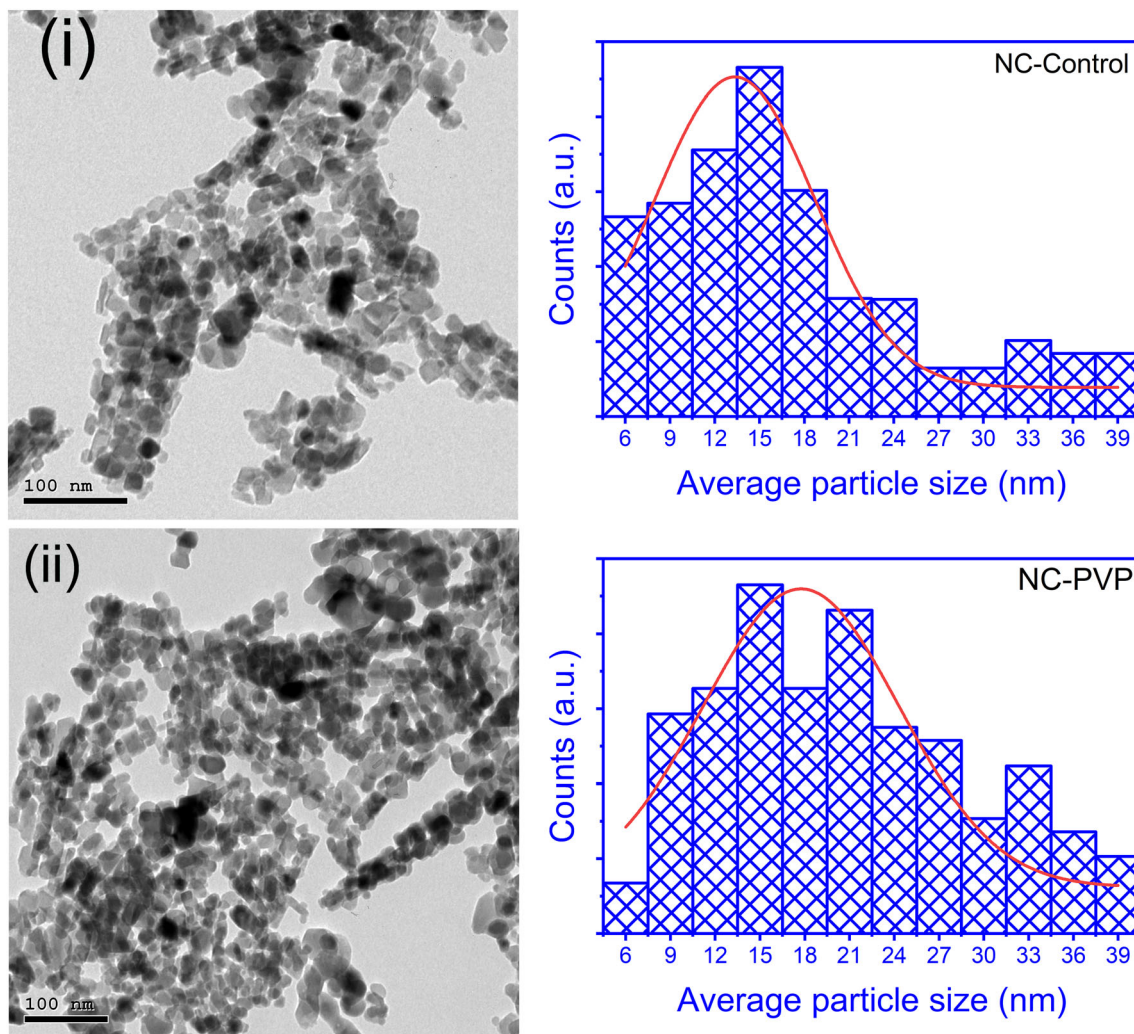


**Fig. 7** HR-TEM micrographs and the calculated average particle size histograms for  $\text{NiCo}_2\text{O}_4$  nanoparticles for: i—NC-Control and ii—NC-PVP



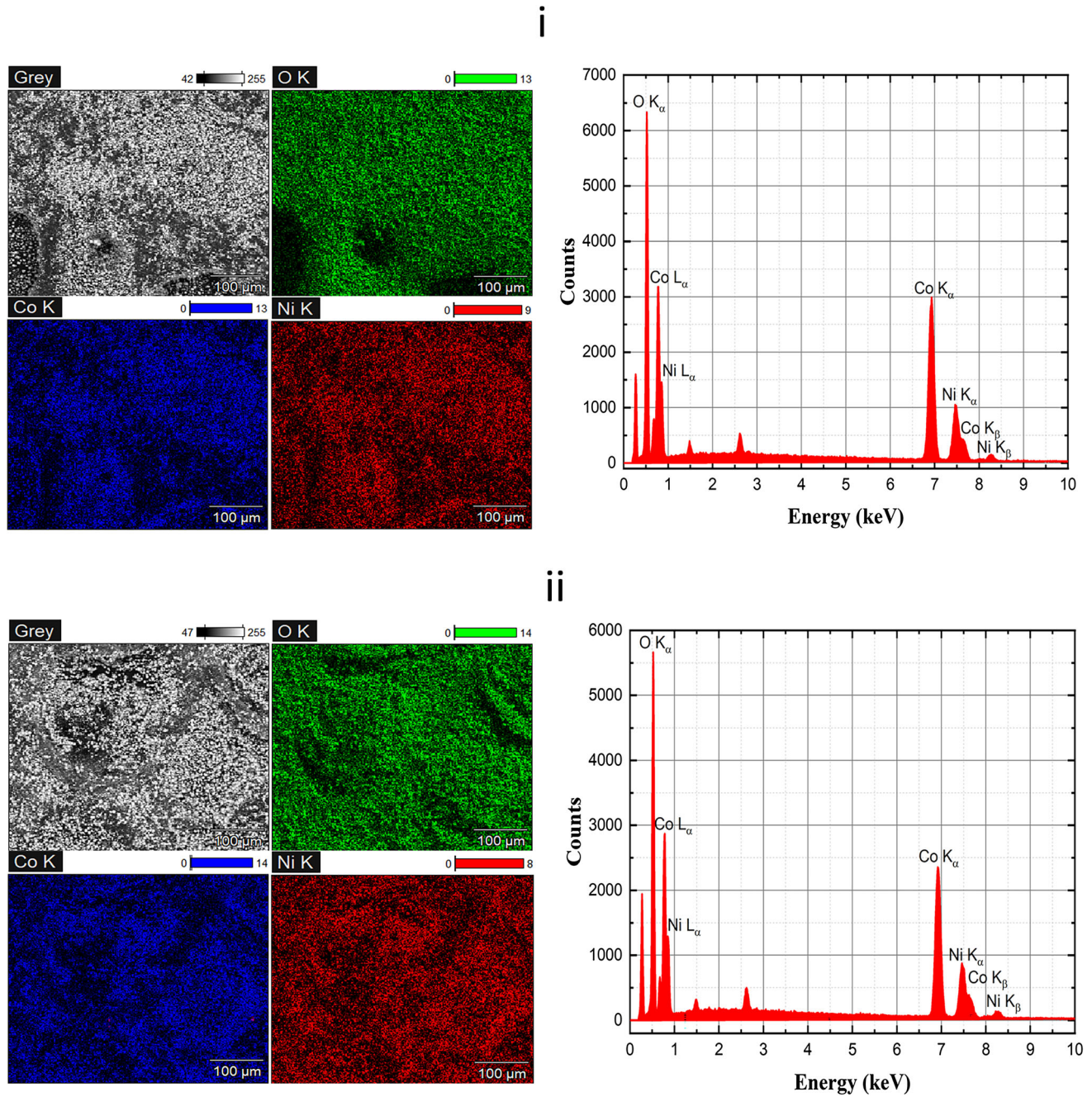


**Fig. 8** SEM mapping and EDX spectra for NiCo<sub>2</sub>O<sub>4</sub> nanoparticles demonstrating the distribution of different elements over large area of the sample for i—NC-control, and ii—NC-PVP, respectively.

surface cations when compared with the control sample.

### 3.6 Surface area

The BET surface analysis of the adsorption–desorption isotherms is performed for all NiCo<sub>2</sub>O<sub>4</sub> samples.

The K<sub>α</sub> lines are indexed only for O, Co, and Ni. The peaks attributed to the substrate and K<sub>β</sub>, and L<sub>α</sub> are not indexed for simplicity

The isotherm N<sub>2</sub> adsorption–desorption curves are presented in Fig. 9 and the hysteresis curves develop approximate behavior H3 isotherm [41, 42]. The behavior of the samples develops a closed hysteresis with enclosed area at P/P<sub>o</sub> > 0.7 without any tendency to saturation, the adsorption–desorption curves merge together at low P/P<sub>o</sub> values except for

**Table 4** EDX analysis for NiCo<sub>2</sub>O<sub>4</sub> nanoparticles

Element	NC-Control		NC-PVP	
	Weight %	Atomic %	Weight %	Atomic %
O	20.34	48.44	18.04	44.67
Ni	56.88	14.78	22.44	15.18
Co	22.78	36.77	59.52	40.15

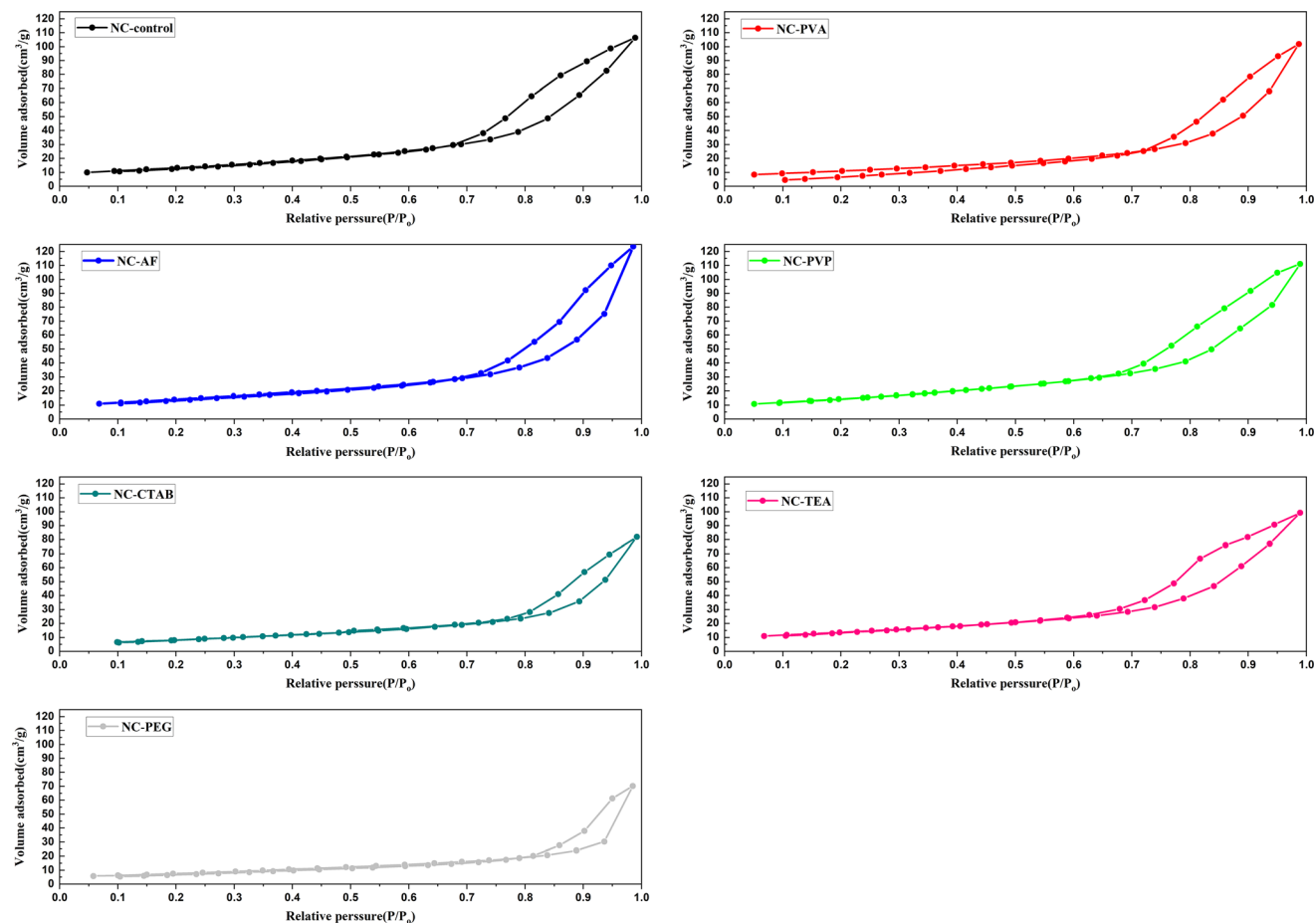
NC-PVA sample (this splitting may be attributed to unsuitable measurement conditions like degassing temperature of the sample, without any physical significance). Hysteresis loops observed in the interval of 0.6–1.0  $P/P_0$  fairly agreed with those of Hao et al., [43]. This behavior confirms the mesoporous nature of the samples with developing large slit-shaped pores.

Typical calculations and BET-specific surface area are described in Sect. S2.3. The calculated values of

the specific surface area are gathered in Table 5. NC-AF sample develops the highest BET-specific surface area of 19.38  $\text{m}^2 \text{g}^{-1}$ , while the NC-CTAB sample has the smallest BET surface area of only 9.36  $\text{m}^2 \text{g}^{-1}$ . It is well understood that electrode materials with a huge surface area will supply more electrochemical active sites for fast redox reactions throughout the high-rate charge/discharge [44].

### 3.7 Electrochemical analysis

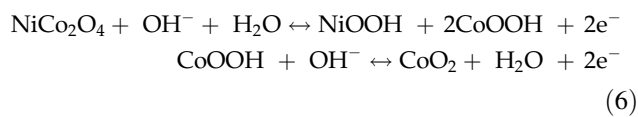
Electrochemical properties of NiCo<sub>2</sub>O<sub>4</sub> samples were described by CV and galvanostatic charge–discharge test in 6.0 M KOH aqueous solution. Figure 10 presents the CV curves corresponding to all the NiCo<sub>2</sub>O<sub>4</sub> samples at different scan rates. A pair of redox peaks appears in each voltammogram, suggesting that the measured capacitance is mainly based on the faradic mechanism. The possible redox reactions are based on the following equations [45]:

**Fig. 9** Nitrogen adsorption–desorption isotherms curves of the NiCo<sub>2</sub>O<sub>4</sub> nanoparticles (control) and with adding some surfactants



**Table 5** BET-specific surface area for the different surfactant/additive modified NiCo<sub>2</sub>O<sub>4</sub> nanoparticles

Sample	Specific surface area (m <sup>2</sup> g <sup>-1</sup> )
NC-control	16.12
NC-PVA	15.64
NC-PVP	16.90
NC-AF	19.38
NC-CTAB	9.36
NC-TEA	15.37
NC-PEG	9.92



The specific capacitances measured from CV curves at different scan rates are shown in Figure 10.

At scan rate of 2 mV s<sup>-1</sup>, the specific capacitance was 458 F g<sup>-1</sup> for NiCo<sub>2</sub>O<sub>4</sub> (control), 212 F g<sup>-1</sup> for NC-PVA, 1180 F g<sup>-1</sup> for NC-PVP, 496 F g<sup>-1</sup> for NC-AF, 443 F g<sup>-1</sup> for NC-CTAB, 261 F g<sup>-1</sup> for NC-TEA, and 306 F g<sup>-1</sup> for NC-PEG. NC-PVP sample shows higher capacitance and an excellent rate capability than other synthesized NiCo<sub>2</sub>O<sub>4</sub> samples. The high performance of NC-PVP sample is attributed to the facile electron conduction along with the urchin-like microspheres with porous surface structures which enhance the pseudocapacitance behavior as well as electric double-layer capacitance (EDLC).

To further evaluate the charge-storage capacity of the prepared electrodes, GCD measurements were performed. Figure 11 shows the GCD curves corresponding to all NiCo<sub>2</sub>O<sub>4</sub> samples with different current densities ranging from 1.0 to 20.0 A g<sup>-1</sup>. From the discharge curves presented in Fig. 11, it can be seen that the fast potential drop was controlled by an

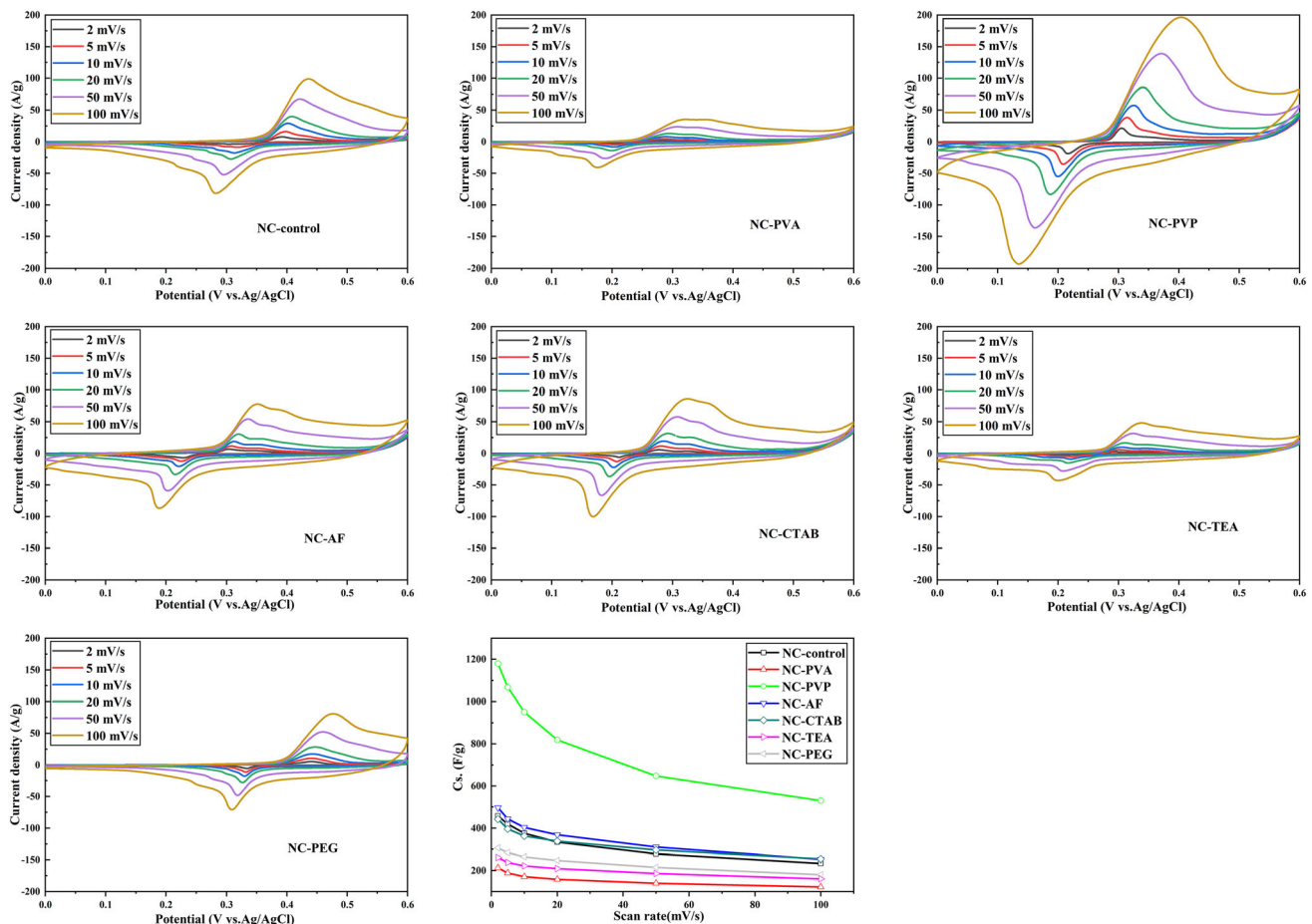


**Fig. 10** CV curves of NiCo<sub>2</sub>O<sub>4</sub> (control), NC-PVA, NC-PVP, NC-AF, NC-CTAB, NC-TEA, and NC-PEG nanoparticle electrodes at different scan rates of 2, 5, 10, 20, 50, 100 mV s<sup>-1</sup>, and the calculated specific capacitance from the CV curves

electric double-layer capacitance. However, the slow potential decay was mainly due to the redox reactions due to the transition of  $\text{Ni}^{2+}/\text{Ni}^{3+}$  and  $\text{Co}^{3+}/\text{Co}^{4+}$ . The specific capacitance values of all  $\text{NiCo}_2\text{O}_4$  samples are calculated from GCD curves and plotted in Figure 11. It is clear that NC-PVP sample demonstrates the highest specific capacitance among other samples, which confirms the CV curves results. The specific capacitance of the NC-PVP electrode was  $2253 \text{ F g}^{-1}$  at  $1 \text{ A g}^{-1}$ . The performance of the NC-PVP sample is superior to that of  $\text{NiCo}_2\text{O}_4$ /mesoporous nanofibers of specific capacitance  $1631 \text{ F g}^{-1}$  at a current density of  $1 \text{ A g}^{-1}$  [46],  $\text{NiCo}_2\text{O}_4$ /GQDs of specific capacitance  $481.4 \text{ F g}^{-1}$  at  $0.35 \text{ A g}^{-1}$  [47],  $\text{MnO}_2/\text{NiCo}_2\text{O}_4/\text{Ni Foam}$  of specific capacitance  $1485.24 \text{ F g}^{-1}$  at  $2 \text{ A g}^{-1}$  [48], and the 3D graphene/ $\text{NiCo}_2\text{O}_4$  film of high specific capacitance of  $708.36 \text{ F g}^{-1}$  at  $1 \text{ A g}^{-1}$  [49]. A comparison with previously reported  $\text{NiCo}_2\text{O}_4$  nanomaterials is also given in Table 6, which further confirms the excellent

performance of the NC-PVP sample. The NC-PVP electrode has a better discharge capacity than any other samples during the charge–discharge process. The result is in good agreement with the observation from CV curves. This should be associated with the synergistic effect of the advantageous structure and large specific surface area. The urchin-like microspheres structure is particularly beneficial for the diffusion of the electrolyte into the inner region of the electrode and the mass transport of the electrolyte within the electrode for fast redox reaction, resulting in the reduced diffusion resistance, high utilization percent of electroactive materials, and enhanced diffusion kinetics. The large surface area and mesoporous structure can help the ions easily transport between 3D materials. In addition, the mesoporous structures in nanowires can greatly increase the electrode/electrolyte contact area, and thus further enhance the electrochemical performance of the electrode.

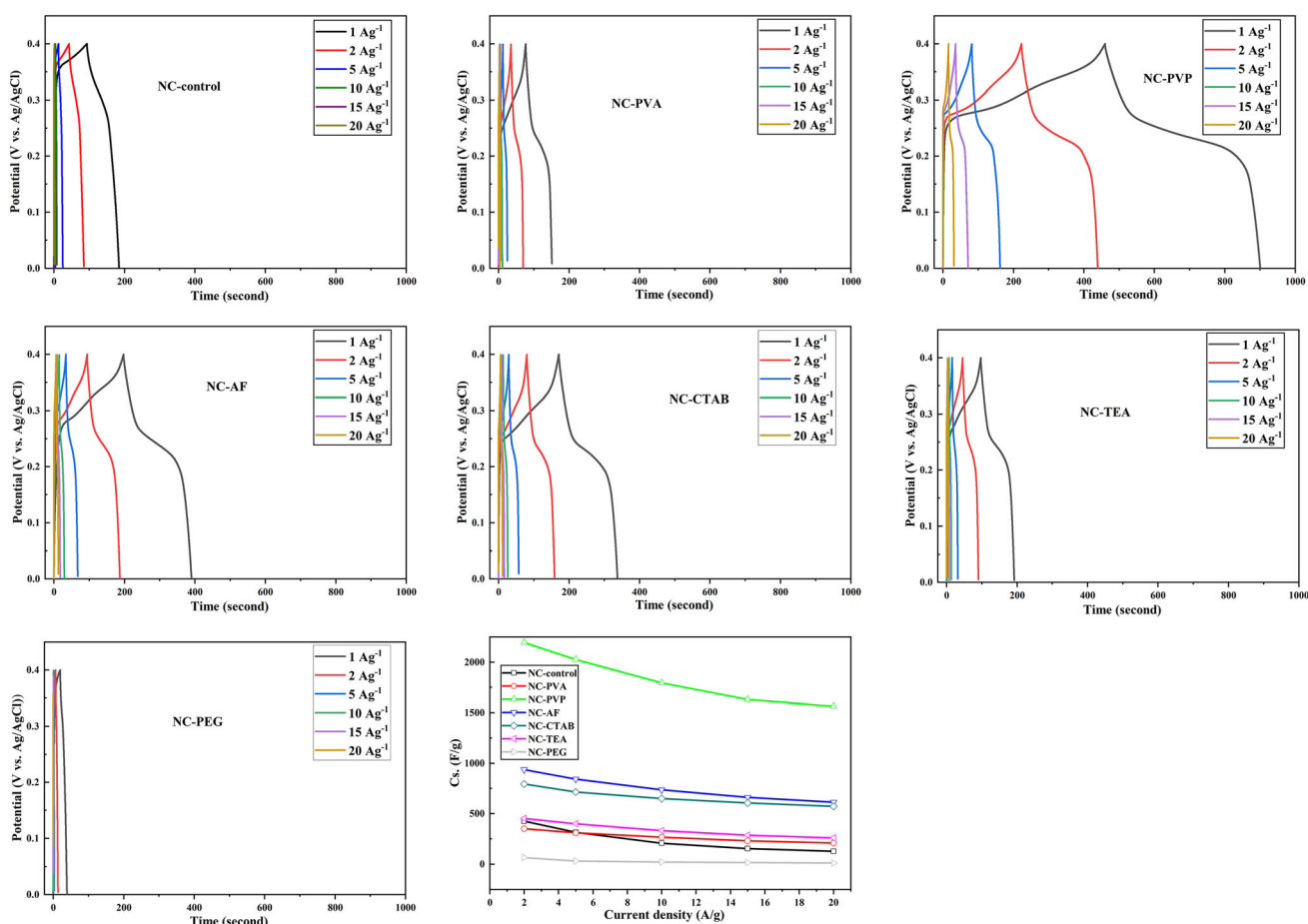


**Fig. 11** GCD curves of  $\text{NiCo}_2\text{O}_4$  (control), NC-PVA, NC-PVP, NC-AF, NC-CTAB, NC-TEA, and NC-PEG nanoparticle electrodes at different current densities of 1, 2, 5, 10, 15,  $20 \text{ A g}^{-1}$ , and the calculated specific capacitance from the GCD curves

**Table 6** Specific capacitance of NiCo<sub>2</sub>O<sub>4</sub> samples obtained in this study, compared with some previously reported results

Material	Specific capacitance	Electrolyte	Retention	Reference
NC-PVP	2253 F g <sup>-1</sup> at 1 A g <sup>-1</sup>	6.0 M KOH	100% after 3200 cycles, 90% after 10,000 cycles	This work
NiCo <sub>2</sub> O <sub>4</sub> /mesoporous nanofibers	1631 F g <sup>-1</sup> at 1 A g <sup>-1</sup>	6.0 M KOH	94.5% after 5000 cycles	[46]
NiCo <sub>2</sub> O <sub>4</sub> /GQDs	481.4 F g <sup>-1</sup> at 0.35 A g <sup>-1</sup>	0.1 M KOH	65.88% after 300 cycles	[47]
MnO <sub>2</sub> /NiCo <sub>2</sub> O <sub>4</sub> /Ni Foam	1485.24 F g <sup>-1</sup> at 2 A g <sup>-1</sup>	1.0 M Na <sub>2</sub> SO <sub>4</sub>	87.5% after 3000 cycles	[48]
3D graphene/NiCo <sub>2</sub> O <sub>4</sub> film	708.36 F g <sup>-1</sup> at 1 A ssg <sup>-1</sup>	1.0 M KOH	94.3% after 6000	[49]

It is worth noting that the decrease of the specific capacitance was reduced during increasing either the scan rate or current density. The high SC observed at the low scan rate (low current density) may be due to the high accessibility of the electrolyte ions to the electrode surface during the faradaic process. Meanwhile, the low accessibility of the electrolyte ions to the electrode surface leads to a slow faradaic reaction at the high scan rate (high current density).

The electrochemical activity is further confirmed by electrochemical impedance spectroscopy (EIS) measurement as shown in Fig. 12i, ii. EIS was evaluated in the frequency range from 10 mHz to 100 kHz at open circuit potential with an amplitude of 10 mV.  $Z'$  and  $Z''$  represent the real and imaginary parts of the impedance, respectively. As can be seen, the Nyquist plot of each sample displays a linear part in the low-frequency region and a semicircle in the high-frequency region. The intersection of the plots at the X-axis represents the equivalent series resistance (ESR). Usually, this resistance is the combination of ionic resistance of the electrolyte, intrinsic resistance of the active material, and contact resistance between the active material and the current collector. In the high-frequency region, the diameter of the semicircle presents the charge transfer resistance ( $R_{ct}$ ) in the electrochemical system, which is associated with the diffusion of charge [43, 45]. As indicated in Fig. 12ii, ESR for the NC-PVP electrode has the lowest value compared with other electrode materials. This behavior is ascribed to the better interface between the electrode and the electrolyte due to the urchin-like microspheres structure. Also, the diameter of the semicircle decreases for the NC-PVP electrode and increases for the other electrodes. This phenomenon is attributed to the different specific surface areas and dispersibility of the urchin-like microspheres structure. Among these electrodes, the NC-PVP electrode

has the smallest ESR and  $R_{ct}$ , implying the easy and fast penetration of the electrolyte ions into the inner layer of the urchin-like microspheres with porous surface NiCo<sub>2</sub>O<sub>4</sub> structure.

The cycling stability of the NC-PVP sample was evaluated by repeating the GCD test between 0 and 0.4 V at a high current density of 10 A g<sup>-1</sup> for 10,000 cycles. Figure 12iii shows that the NC-PVP electrode keeps 100% of its initial capacitance for 3200 cycles, then gradually decreases to 90% of its original capacitance up to 10,000 cycles. Also, the charging/discharging time was almost the same before and after the cycling test which leads to ideal coulombic efficiency. The long-term stability of the NC-PVP electrode material confirms the good electrochemical performance of the urchin-like microspheres with porous surface NiCo<sub>2</sub>O<sub>4</sub> structure.

#### 4 Summary and Conclusion

NiCo<sub>2</sub>O<sub>4</sub> nanoparticles were synthesized by the hydrothermal method. The effect of low concentration additives/surfactants on the physical properties of the nanoparticles is investigated for identical synthesis conditions. Thermal analysis indicated decomposition of precursors into pure oxides with the removal of any apparent residuals after annealing at a temperature ~ 350 °C for all the samples. The XRD patterns revealed that the structure of the annealed samples is single-phase Fd-3m spinel with an average crystallite size within the nanoscale (12–16 nm). The selected surfactants did not affect the lattice parameters significantly and resulted in increasing the average particle size when compared to the control sample. Further, the FTIR results confirmed the formation of the spinel cobaltite. NiCo<sub>2</sub>O<sub>4</sub> nanoparticles with PVP surfactant showed urchin-

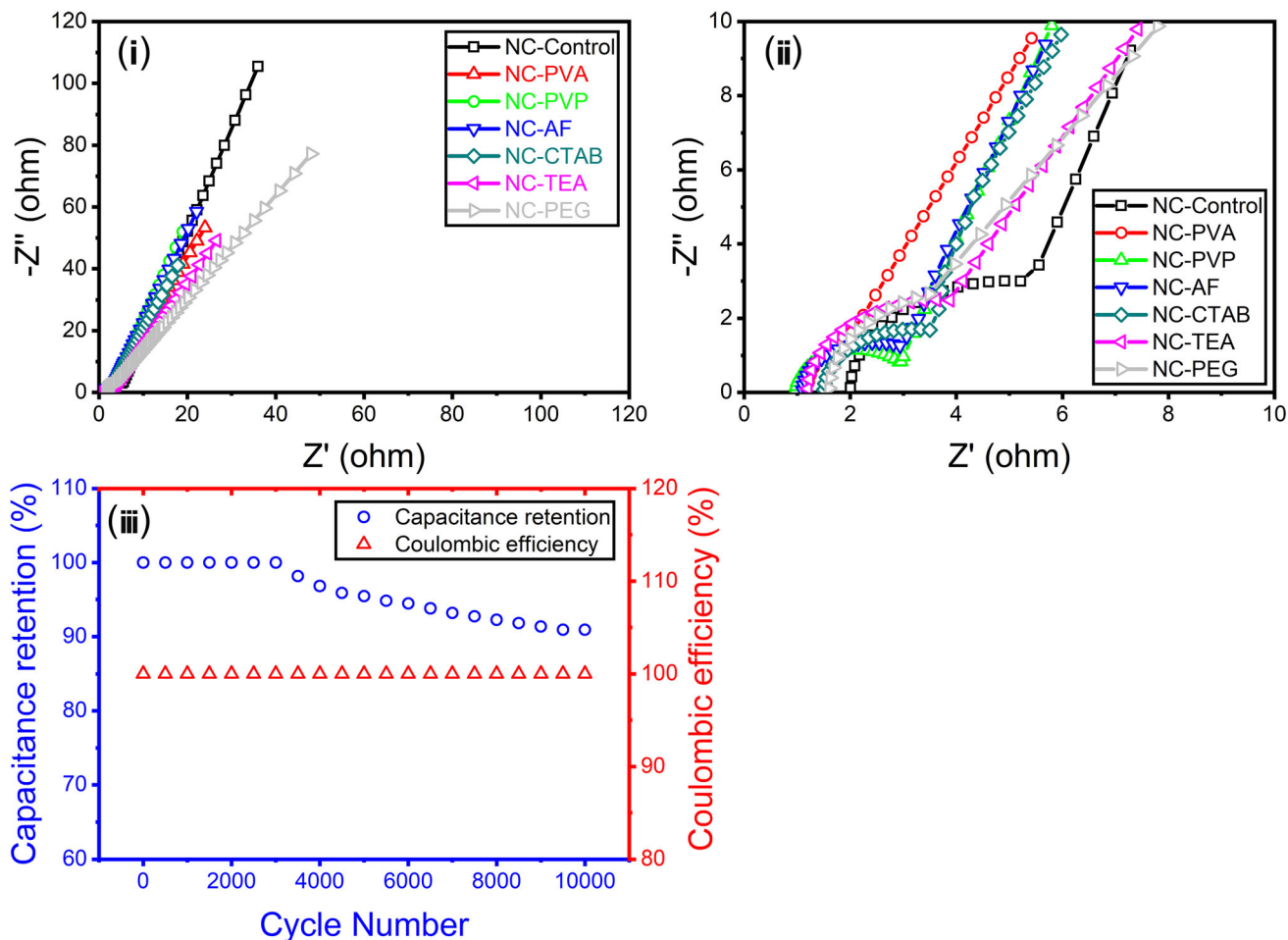


**Fig. 12** i—Nyquist plots, ii—the enlarged Nyquist plots for different electrodes, and iii—cycling stability of the NC-PVP electrode at current density of  $10 \text{ A g}^{-1}$

like microspheres porous structure. This structure had a high electrochemical performance for supercapacitor electrode of  $2253 \text{ Fg}^{-1}$  specific capacitance at  $1 \text{ A g}^{-1}$  and long-term cyclic stability for 10,000 cycles with 90% capacitance retention, which makes it a promising electrode material for high-performance supercapacitors.

### Authors contributions

All authors contributed to the study's conception and design. Material preparation, thermal and structural data collection, and analysis were performed by [HRM] and [AMN]. The electrochemical investigations were performed and analyzed by [MMMM]. The first data draft was revised by [GA] and the

whole project was under the supervision of [AAEF]. All authors read and approved the final manuscript.

### Funding

Open access funding provided by The Science, Technology & Innovation Funding Authority (STDF) in cooperation with The Egyptian Knowledge Bank (EKB).

### Data availability

The datasets generated during and/or analyzed during the current study are available from the corresponding author on reasonable request.



## Declarations

**Conflict of interest** The authors declare that they have no conflict of interest.

**Open Access** This article is licensed under a Creative Commons Attribution 4.0 International License, which permits use, sharing, adaptation, distribution and reproduction in any medium or format, as long as you give appropriate credit to the original author(s) and the source, provide a link to the Creative Commons licence, and indicate if changes were made. The images or other third party material in this article are included in the article's Creative Commons licence, unless indicated otherwise in a credit line to the material. If material is not included in the article's Creative Commons licence and your intended use is not permitted by statutory regulation or exceeds the permitted use, you will need to obtain permission directly from the copyright holder. To view a copy of this licence, visit <http://creativecommons.org/licenses/by/4.0/>.

## References

1. J. Wu, W.M. Lau, D.S. Geng, Recent progress in cobalt-based compounds as high-performance anode materials for lithium ion batteries. *Rare Met.* (2017). <https://doi.org/10.1007/s12598-017-0904-y>
2. Z. Gao, W. Yang, J. Wang, N. Song, X. Li, Flexible all-solid-state hierarchical NiCo<sub>2</sub>O<sub>4</sub>/porous graphene paper asymmetric supercapacitors with an exceptional combination of electrochemical properties. *Nano Energy* (2015). <https://doi.org/10.1016/j.nanoen.2015.02.036>
3. Y. Ouyang et al., Hierarchical structure electrodes of NiO ultrathin nanosheets anchored to NiCo<sub>2</sub>O<sub>4</sub> on carbon cloth with excellent cycle stability for asymmetric supercapacitors. *Chem. Eng. J.* **355**, 416–427 (2019). <https://doi.org/10.1016/j.cej.2018.08.142>
4. S.T. Senthilkumar, N. Fu, Y. Liu, Y. Wang, L. Zhou, H. Huang, Flexible fiber hybrid supercapacitor with NiCo<sub>2</sub>O<sub>4</sub> nanograss@carbon fiber and bio-waste derived high surface area porous carbon. *Electrochim. Acta* **211**, 411–419 (2016). <https://doi.org/10.1016/j.electacta.2016.06.059>
5. Y. Feng et al., MOF-derived spinel NiCo<sub>2</sub>O<sub>4</sub> hollow nanocages for the construction of non-enzymatic electrochemical glucose sensor. *Electroanalysis* (2020). <https://doi.org/10.1002/elan.201900558>
6. L. Tao et al., Nanostructured nickel cobaltite antispinel as bifunctional electrocatalyst for overall water splitting. *J. Phys. Chem. C* **121**(46), 25888–25897 (2017). <https://doi.org/10.1021/acs.jpcc.7b08814>
7. S.V. Devaguptapu et al., Morphology control of carbon-free spinel NiCo<sub>2</sub>O<sub>4</sub> catalysts for enhanced bifunctional oxygen reduction and evolution in alkaline media. *ACS Appl. Mater. Interfaces.* (2017). <https://doi.org/10.1021/acsami.7b16389>
8. A. Abu El-Fadl, M. Almokhtar, A.M. Nashaat, “Synthesis, structural, optical, and magnetic properties of ZnCr<sub>2-x</sub>Fe<sub>x</sub>O<sub>4</sub> (0 ≤ x ≤ 0.8) nanoparticles. *Japan. J. Appl. Phys.* (2018). <https://doi.org/10.7567/JJAP.57.075001>
9. Y. Bitla et al., Origin of metallic behavior in NiCo<sub>2</sub>O<sub>4</sub> ferrimagnet. *Sci. Rep.* (2015). <https://doi.org/10.1038/srep15201>
10. Z. Luo et al., Urchin-like NiCo<sub>2</sub>O<sub>4</sub> hollow microspheres with oxygen vacancies synthesized by self-template for supercapacitor. *New J. Chem.* **45**(48), 22748–22757 (2021). <https://doi.org/10.1039/D1NJ04153C>
11. M.M.M. Mohammed, D.M. Chun, Electrochemical performance of few-layer graphene nano-flake supercapacitors prepared by the vacuum kinetic spray method. *Coatings* (2018). <https://doi.org/10.3390/COATINGS8090302>
12. M.A. Yewale et al., Mesoporous hexagonal nanorods of NiCo<sub>2</sub>O<sub>4</sub> nanoparticles via hydrothermal route for supercapacitor application. *Chem. Phys. Lett.* **800**, 139654 (2022). <https://doi.org/10.1016/j.cplett.2022.139654>
13. M.M.M. Mohammed, D.M. Chun, All-solid-state supercapacitor based on MoS<sub>2</sub>—graphite composite prepared by the vacuum kinetic spray method. *J. Therm. Spray Technol.* **28**(5), 963–973 (2019). <https://doi.org/10.1007/S11666-019-00875-Z/FIGURES/8>
14. S. Liu, D. Ni, H.-F. Li, K.N. Hui, C.-Y. Ouyang, S.C. Jun, Effect of cation substitution on the pseudocapacitive performance of spinel cobaltite MCo<sub>2</sub>O<sub>4</sub> (M = Mn, Ni, Cu, and Co). *J. Mater. Chem. A* **6**(23), 10674–10685 (2018). <https://doi.org/10.1039/C8TA00540K>
15. M. Cheng, H. Fan, Y. Song, Y. Cui, R. Wang, Interconnected hierarchical NiCo<sub>2</sub>O<sub>4</sub> microspheres as high-performance electrode materials for supercapacitors. *Dalton Trans.* **46**(28), 9201–9209 (2017). <https://doi.org/10.1039/C7DT01289F>
16. X. Zhang, Y. Zhao, C. Xu, Surfactant dependent self-organization of Co<sub>3</sub>O<sub>4</sub> nanowires on Ni foam for high performance supercapacitors: from nanowire microspheres to nanowire paddy fields. *Nanoscale* **6**(7), 3638–3646 (2014). <https://doi.org/10.1039/C3NR06734C>
17. X. Zhang, Y. Zhou, B. Luo, H. Zhu, W. Chu, K. Huang, Microwave-assisted synthesis of NiCo<sub>2</sub>O<sub>4</sub> double-shelled hollow spheres for high-performance sodium ion batteries. *Nano-Micro Lett.* **10**(1), 1–7 (2018). <https://doi.org/10.1007/s40820-017-0164-2>

18. B. Cui, H. Lin, J.B. Li, X. Li, J. Yang, J. Tao, Core-ring structured NiCo<sub>2</sub>O<sub>4</sub> nanoplatelets: Synthesis, characterization, and electrocatalytic applications. *Adv. Func. Mater.* **18**(9), 1440–1447 (2008). <https://doi.org/10.1002/adfm.200700982>
19. M.-C. Liu et al., A sol-gel process for the synthesis of NiCo<sub>2</sub>O<sub>4</sub> having improved specific capacitance and cycle stability for electrochemical capacitors. *J. Electrochem. Soc.* (2012). <https://doi.org/10.1149/2.057208jes>
20. N. Wang, B. Sun, P. Zhao, M. Yao, W. Hu, S. Komarneni, Electrodeposition preparation of NiCo<sub>2</sub>O<sub>4</sub> mesoporous film on ultrafine nickel wire for flexible asymmetric supercapacitors. *Chem. Eng. J.* (2018). <https://doi.org/10.1016/j.ccej.2018.03.147>
21. S. Trivedi, R. Prasad, Choice of precipitant and calcination temperature of precursor for synthesis of NiCo<sub>2</sub>O<sub>4</sub> for control of CO–CH<sub>4</sub> emissions from CNG vehicles. *J. Environ. Sci. (China)* (2018). <https://doi.org/10.1016/j.jes.2017.03.002>
22. V. Shanmugavalli, K. Vishista, Low-cost synthesis of cubic spinel structured high efficient NiCo<sub>2</sub>O<sub>4</sub>/polyaniline nanocomposite for supercapacitor application. *Mater. Res. Express* (2019). <https://doi.org/10.1088/2053-1591/aae8ee>
23. R. Jia et al., Self-healable wire-shaped supercapacitors with two twisted NiCo<sub>2</sub>O<sub>4</sub> coated polyvinyl alcohol hydrogel fibers. *Sci. China Mater.* (2018). <https://doi.org/10.1007/s40843-017-9177-5>
24. Y. Yan, G. Cheng, P. Wang, D. He, R. Chen, Facile hydrothermal selective fabrication of Ni(OH)<sub>2</sub> and Ni(HCO<sub>3</sub>)<sub>2</sub> nanoparticulates and their electrochemical performances. *RSC Adv.* (2014). <https://doi.org/10.1039/c4ra06839d>
25. X. Xiong et al., Three-dimensional ultrathin Ni(OH)<sub>2</sub> nanosheets grown on nickel foam for high-performance supercapacitors. *Nano Energy* (2015). <https://doi.org/10.1016/j.nanoen.2014.10.029>
26. S. Min, C. Zhao, Z. Zhang, G. Chen, X. Qian, Z. Guo, Synthesis of Ni(OH)<sub>2</sub>/RGO pseudocomposite on nickel foam for supercapacitors with superior performance. *J. Mater. Chem. A* (2015). <https://doi.org/10.1039/c4ta06233g>
27. K. Yang et al., Yolk-shell bimetallic metal-organic frameworks derived multilayer core-shells NiCo<sub>2</sub>O<sub>4</sub>/NiO structure spheres for high-performance supercapacitor. *J. Electroanal. Chem.* **851**, 113445 (2019)
28. S. Zhan, Z. Zhou, M. Liu, Y. Jiao, H. Wang, 3D NiO nanowalls grown on Ni foam for highly efficient electro-oxidation of urea. *Catal. Today* **327**, 398–404 (2019)
29. X. Xu, Y. Zhao, Q. Lai, Y. Hao, Effect of polyethylene glycol on phase and morphology of calcium carbonate. *J. Appl. Polym. Sci.* **119**(1), 319–324 (2011)
30. J. Rodríguez-Carvajal, FULLPROF: a program for rietveld refinement and pattern matching analysis abstracts of the satellite meeting on powder diffraction of the XV congress of the IUCr. *Physica B.* 1990.
31. C. Hao, S. Zhou, J. Wang, X. Wang, H. Gao, C. Ge, Preparation of hierarchical spinel NiCo<sub>2</sub>O<sub>4</sub> nanowires for high-performance supercapacitors. *Ind. Eng. Chem. Res.* **57**(7), 2517–2525 (2018)
32. A.K. Yedluri, H.-J. Kim, Enhanced electrochemical performance of nanoplate nickel cobaltite (NiCo<sub>2</sub>O<sub>4</sub>) supercapacitor applications. *RSC Adv* **9**(2), 1115–1122 (2019)
33. X. Chen et al., Synthesis and characterization of a NiCo<sub>2</sub>O<sub>4</sub>@NiCo<sub>2</sub>O<sub>4</sub> hierarchical mesoporous nanoflake electrode for supercapacitor applications. *Nanomaterials* (2020). <https://doi.org/10.3390/nano10071292>
34. A.K. Yedluri, H.J. Kim, Enhanced electrochemical performance of nanoplate nickel cobaltite (NiCo<sub>2</sub>O<sub>4</sub>) supercapacitor applications. *RSC Adv.* **9**(2), 1115–1122 (2019). <https://doi.org/10.1039/c8ra09081e>
35. K. Momma, F. Izumi, VESTA 3 for three-dimensional visualization of crystal, volumetric and morphology data. *J. Appl. Crystallogr.* (2011). <https://doi.org/10.1107/S0021889811038970>
36. D. Nath, F. Singh, R. Das, X-ray diffraction analysis by Williamson-Hall, Halder-Wagner and size-strain plot methods of CdSe nanoparticles- a comparative study. *Mater. Chem. Phys.* (2020). <https://doi.org/10.1016/j.matchemphys.2019.122021>
37. R.S. Liu et al., Chemical pressure induced phase transition in single and double perovskites with magnetoresistance effect. *Tamkang J. Sci. Eng.* **5**, 59–61 (2002)
38. K. Manjunatha, V. Jagadeesha Angadi, R. Rajaramakrishna, U. Mahaboob Pasha, Role of 5 mol% Mg-Ni on the structural and magnetic properties of cobalt chromates crystallites prepared by solution combustion technique. *J. Superconduct. Novel Magnet.* **33**(9), 2861–2866 (2020). <https://doi.org/10.1007/s10948-020-05549-4>
39. C. Stella, N. Soundararajan, K. Ramachandran, Structural, optical, and magnetic properties of Mn and Fe-doped Co<sub>3</sub>O<sub>4</sub> nanoparticles. *AIP Adv.* (2015). <https://doi.org/10.1063/1.4928218>
40. S.A. Mazen, M.H. Abdallah, R.I. Nakhla, H.M. Zaki, F. Metawe, X-ray analysis and IR absorption spectra of Li-Ge ferrite. *Mater. Chem. Phys.* (1993). [https://doi.org/10.1016/0254-0584\(93\)90116-4](https://doi.org/10.1016/0254-0584(93)90116-4)
41. S.J. Gregg, K.S.W. Sing, H.W. Salzberg, Adsorption surface area and porosity. *J. Electrochem. Soc.* **114**(11), 279C (1967)
42. K.S.W. Sing, Reporting physisorption data for gas/solid systems with special reference to the determination of surface area and porosity (Recommendations 1984). *Pure Appl.*

- Chem. **57**(4), 603–619 (1985). <https://doi.org/10.1351/pac198557040603/pdf?stream=true>
43. C. Huang et al., PVP-assisted growth of Ni-Co oxide on N-doped reduced graphene oxide with enhanced pseudocapacitive behavior. *Chem. Eng. J.* **378**, 122202 (2019). <https://doi.org/10.1016/J.CEJ.2019.122202>
44. K. Chen, D. Xue, Searching for electrode materials with high electrochemical reactivity. *J. Materiom.* **1**(3), 170–187 (2015). <https://doi.org/10.1016/J.JMAT.2015.07.001>
45. I. Shakir, High performance flexible pseudocapacitor based on nano-architected spinel nickel cobaltite anchored multiwall carbon nanotubes. *Electrochim. Acta* **132**, 490–495 (2014). <https://doi.org/10.1016/J.ELECTACTA.2014.03.138>
46. Y. Yang, D. Zeng, S. Yang, L. Gu, B. Liu, S. Hao, Nickel cobaltite nanosheets coated on metal-organic framework-derived mesoporous carbon nanofibers for high-performance pseudocapacitors. *J. Colloid Interface Sci.* **534**, 312–321 (2019). <https://doi.org/10.1016/J.JCIS.2018.09.037>
47. P.R. Kharangarh, N.M. Ravindra, R. Rawal, A. Singh, V. Gupta, Graphene quantum dots decorated on spinel nickel cobaltite nanocomposites for boosting supercapacitor electrode material performance. *J. Alloys Compd.* **876**, 159990 (2021). <https://doi.org/10.1016/J.JALLCOM.2021.159990>
48. B. Tao, J. He, F. Miao, Y. Zhang, MnO<sub>2</sub>/NiCo<sub>2</sub>O<sub>4</sub> loaded on nickel foam as a high-performance electrode for advanced asymmetric supercapacitor. *Vacuum* **195**, 110668 (2022). <https://doi.org/10.1016/J.VACUUM.2021.110668>
49. Y. Zhou, Z. Huang, H. Liao, J. Li, H. Wang, Y. Wang, 3D porous graphene/NiCo<sub>2</sub>O<sub>4</sub> hybrid film as an advanced electrode for supercapacitors. *Appl. Surf. Sci.* **534**, 147598 (2020). <https://doi.org/10.1016/J.APSUSC.2020.147598>

**Publisher's Note** Springer Nature remains neutral with regard to jurisdictional claims in published maps and institutional affiliations.